

Exact solutions for the wrinkle patterns of confined elastic shells

Ian Tobasco,^{1,*} Yousra Timounay,^{2,3} Desislava Todorova,⁴
Graham C. Leggat,² Joseph D. Paulsen,^{2,3,†} and Eleni Katifori^{4,‡}

¹*Department of Mathematics, Statistics, and Computer Science,
University of Illinois at Chicago, Chicago, IL 60607, USA*

²*Department of Physics, Syracuse University, Syracuse, NY 13244, USA*

³*BioInspired Syracuse: Institute for Material and Living Systems, Syracuse University, Syracuse, NY 13244, USA*

⁴*Department of Physics and Astronomy, University of Pennsylvania, Philadelphia, PA 19104, USA*

Thin elastic membranes form complex wrinkle patterns when put on substrates of different shapes [1–7]. Such patterns continue to receive attention across science and engineering [8–13]. This is due, in part, to the promise of lithography-free micropatterning [14–17], but also to the observation that similar patterns arise in biological systems from growth [18–22]. The challenge is to explain the patterns in any given setup, even when they fail to be robust. Building on the theoretical foundation of [23], we derive a complete and simple rule set for wrinkles in the model system of a curved shell on a liquid bath. Our rules apply to shells whose initial Gaussian curvatures are of one sign, such as cutouts of saddles and spheres. They predict the surprising coexistence of orderly wrinkles alongside disordered regions where the response appears stochastic, which we confirm in experiment and simulation. They also unveil the role of the shell’s medial axis, a distinguished locus of points that we show is a basic driver in pattern selection. Finally, they explain how the sign of the shell’s initial curvature dictates the presence or lack of disorder. Armed with our simple rules, and the methodology underlying them, one can anticipate the creation of designer wrinkle patterns.

Consider an initially curved elastic shell that adheres to an otherwise planar liquid bath, as in Fig. 1a,b. There, shapes (squares) are cut out of saddle and spherical shells, and subsequently confined to the bath. It is a basic fact of geometry that no length-preserving map exists from a naturally curved surface to the plane. This incompatibility manifests as a mechanical instability leading to wrinkles. Fig. 3 shows the patterns produced by numerous cut out shapes, including triangles and rectangles and other less symmetric shapes as well. The layout of the wrinkles depends strongly on the shape, as well as on the sign of the initial Gaussian curvature κ , which is < 0 for a saddle and > 0 for a sphere. Complicating things further, the typical spherical shell exhibits a mixed “ordered–disordered” response in which the wrinkles are robust to perturbations and similar between trials outside of a disordered core. There, the response is sensitive to perturbations and changes between trials (e.g., the central diamond in Fig. 1b is disordered). At first, predicting

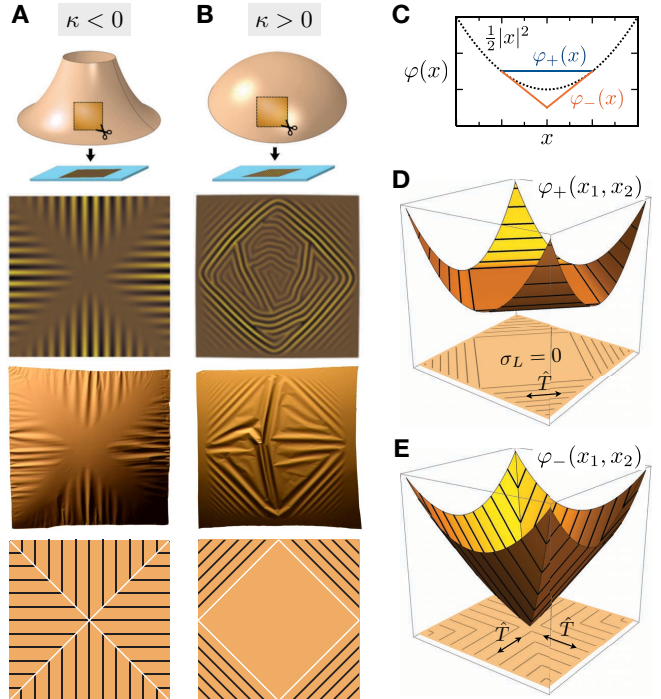


FIG. 1. Wrinkling of confined shells. Wrinkle patterns result when cutouts (squares) from saddle-shaped (A) and spherical (B) shells are forced flat. Simulations and experiments in that order show regions of robust wrinkles, coexisting in some cases with a disordered core as in (B). The medial axis is the white X in (A). (C–E): The patterns are found by projecting the ruling lines of the largest and smallest convex extensions $\varphi_+(x)$ and $\varphi_-(x)$ of $(x_1^2 + x_2^2)/2$ into the square.

the wrinkles of any given shell may seem a hopeless task. Actually, as we show, they follow a simple set of rules.

Look first at the wrinkles of the initially saddle-shaped cutouts in Figs. 1–3 ($\kappa < 0$). Their wrinkles follow *paths of quickest exit* from the cut out shape. Such paths are line segments that meet the boundary perpendicularly, and meet each other at the *medial axis* or *skeleton* of the shell—the locus of points equidistant by closest approach to multiple boundary points, shown in white. Now look at the spherical cutouts ($\kappa > 0$). Their wrinkles are also set by the medial axis, although this may not be immediately clear. The key is Fig. 2, which reveals that the wrinkles of saddle and spherical shells come in *reciprocal pairs*.

* itobasco@uic.edu

† jdpaulse@syr.edu

‡ katifori@sas.upenn.edu

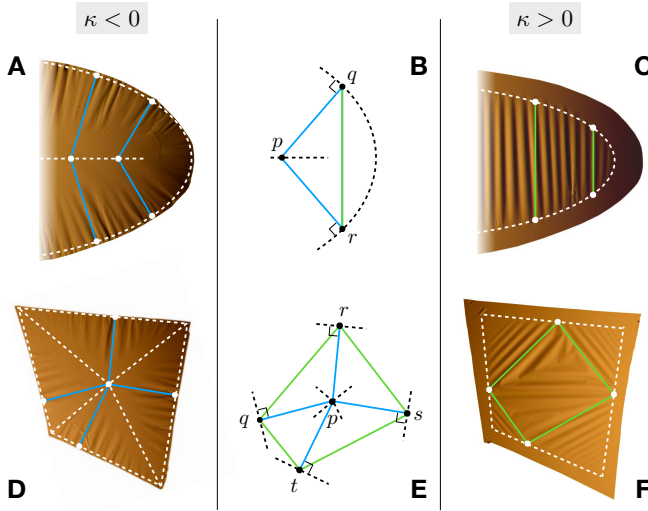


FIG. 2. Reciprocal rules for wrinkles. (A-C): Ordered wrinkles in saddle and spherical shells (right halves of ellipses shown). Their wrinkles pair to form isosceles triangles (B). In particular, point p on the medial axis is closest to two boundary points q, r . For the saddle cutout (A), wrinkles fall along the blue segments pq, pr ; for the spherical cutout (C), the green segment qr is along the wrinkles. (D-F): Finding the disorder. Point p on the medial axis is closest to more than two boundary points. For the saddle cutout (D), wrinkles occur along the blue segments pq, pr, ps, pt . For the spherical cutout (F), the green polygon $qrst$ is disordered.

Most points p on the medial axis have exactly two closest boundary points, called q and r in panel (b). While saddle-shaped cutouts wrinkle along the segments pq and pr , spherical cutouts wrinkle along qr instead. Taken together, the ordered wrinkles of saddle and spherical shells form a family of isosceles triangles. Disordered regions correspond to those exceptional points p on the medial axis with three or more closest boundary points. Panel (e) shows one such p and its closest boundary points q, r, s , and t . While pq, pr, ps , and pt are along the wrinkles of the saddle cutout, the polygon $qrst$ is disordered for its spherical twin. The possibility of infinitely many closest boundary points occurs for the spherical disc in Fig. 3, which is totally disordered save for a small rim.

Below, we give a general derivation of these rules, which successfully capture the wrinkle patterns of the hundreds of shells tested in experiment and simulation. In the experiment, polystyrene films ($E = 3.4$ GPa, $\nu = 0.34$) of thickness $120 < t < 430$ nm are spin-coated on spherical and saddle-shaped glass substrates with principal radii of curvature $13 < R < 39$ mm. Cutouts of width $2.5 < W < 16$ mm are released to a flat air–water interface with surface tension $\gamma_{lv} = 0.072$ N/m and gravitational stiffness $K = \rho g$. The experiments reside in the limit of weak tension $\gamma_{lv}R^2 \ll YW^2$, moderately stiff substrate $KW^2 \gtrsim \gamma_{lv}$, and negligible bending stiffness $BKR^4 \ll Y^2W^4$ where $Y = Et$ and $B = Et^3/12(1 - \nu^2)$

are the stretching and bending moduli. Being shallow yet much larger than the characteristic substrate-dominated wrinkle wavelength, $(B/K)^{1/4} \ll W \ll R$, the cutouts adopt a roughly planar shape and wrinkle as in Figs. 1-3.

At the same time, we perform ABAQUS simulations in a similar parameter regime, though with the surface tension set to zero so that no forces are applied at the lateral boundary of the shell. The result is a “softly stamped” version of the well-known example of a plate pressed into a hard spherical mold [1, 7]. Similar patterns arise in the simulation and the experiment, with the layout of the ordered regions and the location of the disordered regions the same (in Fig. 1a,b, the second row from the top shows simulations). The conclusion, which should be compared against the paradigm of tension-field theory [24–26] as a way of understanding the gross features of wrinkle patterns, is that even in the absence of tensile boundary forces, the patterns persist (see also [7, 23]). We also simulate shells with non-constant initial Gaussian curvature $\kappa(x)$. So long as $\kappa(x)$ is of a definite sign, the patterns remain essentially the same as for their spherical and saddle counterparts (see Fig. S1 in the Supplementary Information). We turn to explain these remarkably robust features of geometry-driven wrinkling.

In principle, one starts by minimizing the elastic energy of bending and stretching the shell, along with the energy of the bath (with or without surface energy). We posit that the layout of the patterns are governed by the following geometry problem instead: find the deformation of the shell to the plane that maximizes the area it covers, under the constraint that it can compress but cannot stretch. To help visualize this *maximum coverage problem*, imagine projecting a curved shell directly to the plane. While the compression that results can be relieved by wrinkles, it can also be reduced by boundary displacements that help the shell “get out of its own way”. Such displacements, while small, can lower the energy. They are limited by the large cost of stretching.

Precisely, we minimize the difference of the initial and covered planar areas of the shell, $\Delta A\{u\} = A_{\text{initial}} - A_{\text{covered}}\{u\}$, while keeping its displacement tension-free:

$$\min_{u(x)} \Delta A\{u\} \quad \text{subject to} \quad \varepsilon(u) \leq 0. \quad (1)$$

The in-plane displacement $u = (u_1(x), u_2(x))$ is a function of the Euclidean coordinate $x = (x_1, x_2)$ in a reference domain $\Omega \subset \mathbb{R}^2$ for the cutout. We use the initial projected shape (e.g., a square). The in-plane strain $\varepsilon_{ij}(u) = (\partial_i u_j + \partial_j u_i - M_{ij})/2$, where $M_{ij} = \partial_i p \partial_j p$. It sets the “geometric misfit” where $p(x)$ is the initial height of the shell, e.g., $\propto x_1^2 + x_2^2$ or $x_1^2 - x_2^2$ for a sphere or a saddle. That $\varepsilon(u) \leq 0$ means its eigenvalues are ≤ 0 .

Similar area-based models have been used before [27–30], but a general first-principles derivation of them is lacking. Ref. [23] derives (1) as the leading order term in an energy expansion obtained via Γ -convergence [31], under an additional assumption on the parameters. Eq. (1) is also consistent with the far-from-threshold expansions

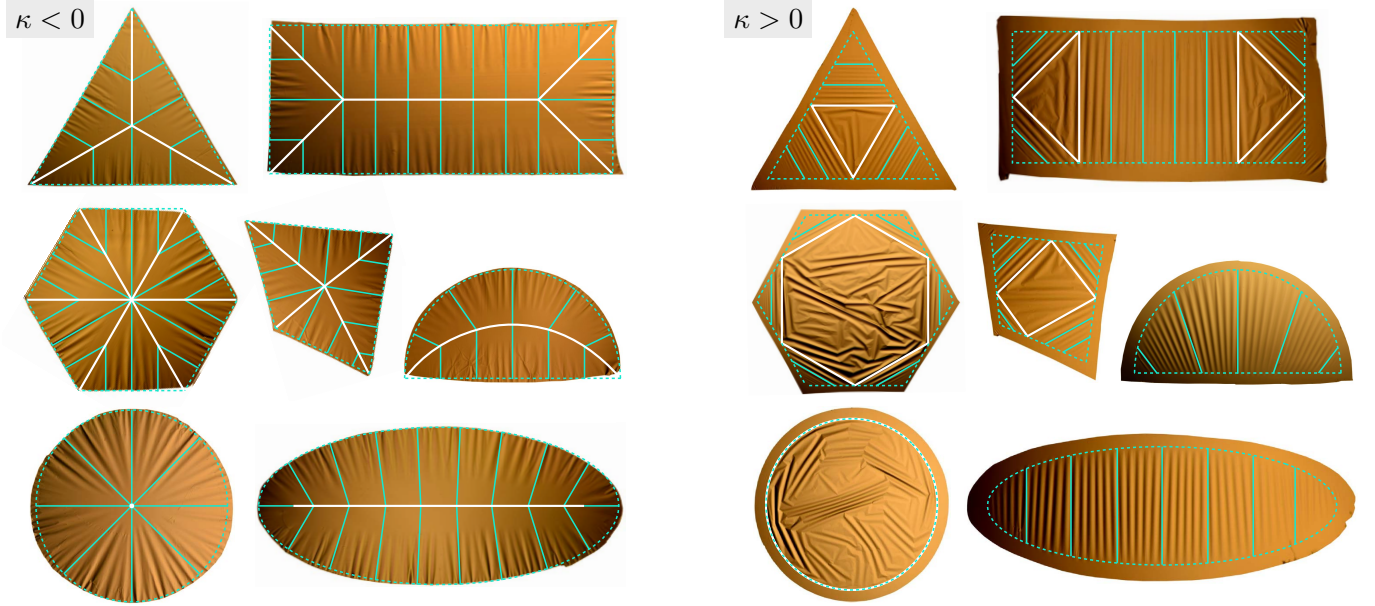


FIG. 3. **Floating shells and their wrinkles.** Solid cyan lines show the predicted wrinkle patterns. Regions absent these lines are disordered. For saddle-shaped ($\kappa < 0$) shells, wrinkles decay towards the medial axis in white. For spherical ($\kappa > 0$) shells, wrinkles decay towards the boundary. Dotted cyan curves show ideal shapes used in the predictions; flattened regions are treated in the coarse-grained theory as infinitesimally fine. Experimental parameters are in Tables SI-SII.

of [7], which are developed for an ordered example akin to our saddle-shaped disc. In any case, the variable $u(x)$ being optimized over in (1) is not the true displacement of the shell, but rather a coarse-grained version obtained by ‘‘averaging out’’ the wrinkles. At finite thickness, defects in the patterns it predicts can occur, similar to [32].

Taking the maximum coverage problem as our starting point, we proceed to solve it for the patterns. We do so indirectly via a Lagrange multipliers approach, where the unknown u is replaced by a two-by-two symmetric matrix-valued function $\sigma_L(x)$. It is a multiplier for the constraint $\varepsilon(u) \leq 0$. We take $\sigma_L \geq 0$ meaning its eigenvalues are ≥ 0 . The crucial mathematical fact is that any displacement u solving (1) must obey

$$\sigma_L : \varepsilon(u) = 0 \quad (2)$$

for a fixed σ_L independent of u . In (2), the notation sums $(\sigma_L)_{ij}\varepsilon_{ij}(u)$ over indices. Geometrically, it says that σ_L and $\varepsilon(u)$ are orthogonal. Their non-null eigendirections must then be orthogonal as well. This is the key to explaining the patterns. Indeed, as $\varepsilon(u)$ is a macroscopic quantity obtained by coarse-graining the wrinkles, its null eigendirections will be along their peaks and troughs. Given a non-null eigendirection $\hat{T}(x)$ of $\sigma_L(x)$, we therefore predict the existence of orderly wrinkles with peaks and troughs along \hat{T} . We call this a *stable direction*, as although tension is not necessarily applied along it, it emerges to set the response anyhow. No stable directions exist where $\sigma_L = 0$, permitting a disordered response.

The question remains how to determine σ_L for a given

shell. For this, we bring in the Lagrangian

$$\mathcal{L}\{u, \sigma_L\} = \Delta A\{u\} + \int_{\Omega} \sigma_L : \varepsilon(u) \quad (3)$$

defined for all $\sigma_L \geq 0$ and u . Solutions of (1) belong to the saddle points of \mathcal{L} [23]. Taking one-sided variations in σ_L yields (2). Taking variations in u gives $\nabla \cdot \sigma_L = 0$. One might expect $\sigma_L \hat{n} = \hat{n}$ at $\partial\Omega$, where \hat{n} is the outwards pointing unit normal. Instead, certain relaxed boundary conditions apply, found by extending $\sigma_L = I$ outside Ω and minimizing (3) in u . We do this in the SI, leading to the following *dual problem* for σ_L :

$$\max_{\sigma_L(x)} -\frac{1}{2} \int_{\Omega} M : (\sigma_L - I). \quad (4)$$

The maximization is over all non-negative σ_L that equal I outside Ω , and are divergence-free.

At this point, our claim has become that the wrinkle patterns of shallow shells confined to a plane are set by σ_L solving (4). In practice, we use a scalar, Airy-like potential $\varphi(x)$ with

$$(\sigma_L)_{11} = \partial_{22}\phi, \quad (\sigma_L)_{22} = \partial_{11}\phi, \quad (\sigma_L)_{12} = -\partial_{12}\phi. \quad (5)$$

The constraints require that φ is a convex function. They also allow us to set $\varphi = (x_1^2 + x_2^2)/2$ outside Ω , in particular because our shells lack holes. We call such φ *convex extensions* of $|x|^2/2$ into Ω . Setting (5) into (4) yields

$$-\frac{1}{2} \int_{\Omega} M : (\sigma_L - I) = \int_{\Omega} (\varphi - \frac{1}{2}|x|^2)\kappa \quad (6)$$

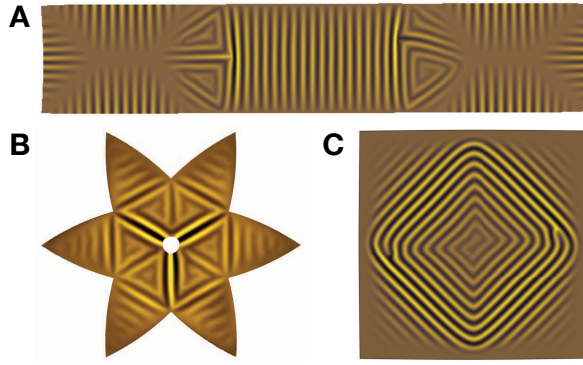


FIG. 4. **Open questions.** While in principle our approach is capable of describing the patterns of (A) shells with initial curvature of varying sign ($\kappa < 0$ on the left and right, > 0 in the middle) and (B) shells with holes ($\kappa > 0$), we presently lack solution formulas in these cases. (C) Another question regards the presence of order in regions consistent with disorder (cf. Fig 1b). Simulation parameters are in Table SIII.

where $\kappa(x)$ is the initial Gaussian curvature. Of immediate interest are shells with $\kappa(x) < 0$ or > 0 everywhere. For these, it is the smallest or largest convex extensions $\varphi_-(x)$ or $\varphi_+(x)$ that maximize (6). These potentials depend only on Ω , as do their multipliers and stable directions. As for $\kappa(x)$, the conclusion is that the patterns depend only on its sign. This explains what might have remained a curious observation from the simulations.

The predictions in Figs. 1 and 3 arose initially in this way, by finding φ_{\pm} for each cutout [23]. Fig. 1c-e depicts this procedure for a square, which we detail in the SI. Fortunately, general solution formulas exist in the form of our simple rules, circumventing the need for a case-by-case analysis. We end by deriving them. Starting with $\kappa(x) < 0$, observe that $\varphi_-(x) = x \cdot P_{\partial\Omega}(x) - |P_{\partial\Omega}(x)|^2/2$ where $P_{\partial\Omega}(x)$ is a closest boundary point to $x \in \Omega$. This is the two-dimensional version of the lower curve in Fig. 1c, and we justify it in the SI. Applying (5) gives

$$\sigma_L = R^T \nabla P_{\partial\Omega} R \quad \text{if } \kappa(x) < 0, \quad (7)$$

where R is a rotation by $\pi/2$. Ordered wrinkles manifest along the stable directions $\hat{T}(x)$ introduced after (2). Here, $\hat{T} \times \nabla P_{\partial\Omega} \neq 0$ and $\hat{T} \cdot \nabla P_{\partial\Omega} = 0$, so directions of constant $P_{\partial\Omega}$ are stable. This shows the wrinkles of negatively curved shells follow paths of quickest exit.

The case $\kappa(x) > 0$ is more involved. The key to solving it lies with the reciprocal rules of Fig. 2. These follow from the beautiful and unexpected fact that φ_+ and φ_- are Legendre transforms of each other, regardless of Ω . We explain why in the SI, where we also show that

$$\sigma_L = R^T \nabla P_{\mathfrak{M}} R \quad \text{if } \kappa(x) > 0. \quad (8)$$

Here, $P_{\mathfrak{M}}(x)$ is a point on the medial axis whose closest boundary points have x in their convex hull—the smallest

convex set including the given boundary points. The points p in Fig. 2b,e show $P_{\mathfrak{M}}(x)$ for x on the segment qr , and for x interior to the polygon $qrst$. Stable directions obey $\hat{T} \times \nabla P_{\mathfrak{M}} \neq 0$ and $\hat{T} \cdot \nabla P_{\mathfrak{M}} = 0$, hence they point along qr and other such segments. No stable directions exist in $qrst$ and other regions where $\nabla P_{\mathfrak{M}} = 0$. These remarks lead at once to our reciprocal rules.

Given the success of our rules in capturing wrinkle patterns, it is natural to think back to other instances of reciprocity and graphical methods in mechanics. A well-known method is due to Maxwell [33], and independently to Taylor, whose reciprocal diagrams of forces and frames encode an elegant test of equilibrium for planar structures (for the history and other examples, see [34]). Recently, these ideas have been used in the computer-aided design of self-supporting structures with specified shapes [35]. To our knowledge, the reciprocity uncovered here between the wrinkles of positively and negatively curved shells is the first such example for elastic patterns. We wonder to what extent it generalizes. Examples of shells for which we lack simple rules are in Fig. 4a,b. Panel (c) highlights the fact that ordered wrinkles sometimes occur in regions consistent with disorder. Empirically, this looks to depend on the finite wrinkle wavelength.

We have shown how to solve for the wrinkles of confined elastic shells, using Lagrange multipliers and, eventually, a simple set of rules. Our results point towards a general, diagrammatic method for benchmarking elastic patterns, which could prove useful for their rapid design. We highlight a promising connection with the little known theory of *ideal locking materials*—bulk materials whose microstructures facilitate extension with negligible stress up to a threshold strain [36]. This limit is apparently approached in biology, by the mesentery membrane of rabbits [37, 38] and the capture silk of some spiders, the latter of which has inspired ultrastretchable wicked membranes [39, 40]. We view the wrinkles of our confined shells as an emergent-yet-sacrificial microstructure enabling them to conform to the plane. We think of σ_L in this connection as the *locking stress*. It is orthogonal to the coarse-grained strain. Whether this description extends beyond the shells treated here remains to be seen.

Acknowledgements. We thank B. Davidovitch, V. Démery, C. R. Doering, G. Francfort, R. D. James, R. V. Kohn, N. Menon, D. Vella, and A. Waas for helpful discussions. This work was supported by NSF awards DMS-1812831 and DMS-2025000 (IT); NSF award DMR-CAREER-1654102 (YT, JDP); NSF award PHY-CAREER-1554887, Univ. of Pennsylvania MRSEC award DMR-1720530 and CEMB award CMMI-1548571, and a Simons Foundation award 568888 (EK).

Author contributions. IT, EK, and JDP conceived and designed the research; IT developed and implemented the theory; DT and EK conducted and analyzed the simulations; YT, GCL, and JDP conducted and analyzed the experiments; IT, YT, DT, EK, and JDP wrote the manuscript.

[1] J. Hure, B. Roman, and J. Bico, “Stamping and wrinkling of elastic plates,” *Phys. Rev. Lett.* **109**, 054302 (2012).

[2] D. Breid and A. J. Crosby, “Curvature-controlled wrinkle morphologies,” *Soft Matter* **9**, 3624–3630 (2013).

[3] N. Stoop, R. Lagrange, D. Terwagne, P. M. Reis, and J. Dunkel, “Curvature-induced symmetry breaking determines elastic surface patterns,” *Nat. Mater.* **14**, 337–342 (2015).

[4] H. Aharoni, D. V. Todorova, O. Albarrán, L. Goehring, R. D. Kamien, and E. Katifori, “The smectic order of wrinkles,” *Nat. Commun.* **8**, 15809 (2017).

[5] P. Bella and R. V. Kohn, “Wrinkling of a thin circular sheet bonded to a spherical substrate,” *Philos. Trans. R. Soc. A* **375**, 20160157 (2017).

[6] X. Zhang, P. T. Mather, M. J. Bowick, and T. Zhang, “Non-uniform curvature and anisotropic deformation control wrinkling patterns on tori,” *Soft Matter* **15**, 5204–5210 (2019).

[7] B. Davidovitch, Y. Sun, and G. M. Grason, “Geometrically incompatible confinement of solids,” *Proc. Natl. Acad. Sci.* **116**, 1483–1488 (2019).

[8] E. Cerdá and L. Mahadevan, “Geometry and physics of wrinkling,” *Phys. Rev. Lett.* **90**, 074302 (2003).

[9] B. Audoly and Y. Pomeau, *Elasticity and geometry: From hair curls to the non-linear response of shells* (Oxford University Press, Oxford, 2010).

[10] H. King, R. D. Schroll, B. Davidovitch, and N. Menon, “Elastic sheet on a liquid drop reveals wrinkling and crumpling as distinct symmetry-breaking instabilities,” *Proc. Natl. Acad. Sci.* **109**, 9716–9720 (2012).

[11] P. M. Reis, “A perspective on the revival of structural (in)stability with novel opportunities for function: From buckliphobia to buckliphilia,” *J. Appl. Mech.* **82**, 111001 (2015).

[12] J. D. Paulsen, “Wrapping liquids, solids, and gases in thin sheets,” *Annu. Rev. Condens. Matter Phys.* **10**, 431–450 (2019).

[13] D. Vella, “Buffering by buckling as a route for elastic deformation,” *Nat. Rev. Phys.* **1**, 425–436 (2019).

[14] M. Pretzl, A. Schweikart, C. Hanske, A. Chiche, U. Zettl, A. Horn, A. Böker, and A. Fery, “A lithography-free pathway for chemical microstructuring of macromolecules from aqueous solution based on wrinkling,” *Langmuir* **24**, 12748–12753 (2008).

[15] S. Yang, K. Khare, and P.-C. Lin, “Harnessing Surface Wrinkle Patterns in Soft Matter,” *Adv. Funct. Mater.* **20**, 2550–2564 (2010).

[16] C.-M. Chen and S. Yang, “Wrinkling instabilities in polymer films and their applications,” *Polym. Int.* **61**, 1041–1047 (2012).

[17] Z. Li, Y. Zhai, Y. Wang, G. M. Wendland, X. Yin, and J. Xiao, “Harnessing surface wrinkling-cracking patterns for tunable optical transmittance,” *Adv. Opt. Mater.* **5**, 1–7 (2017).

[18] E. Sharon, B. Roman, M. Marder, G.-S. Shin, and H. L. Swinney, “Buckling cascades in free sheets,” *Nature* **419**, 579–579 (2002).

[19] A. E. Shyer, T. Tallinen, N. L. Nerurkar, Z. Wei, E. S. Gil, D. L. Kaplan, C. J. Tabin, and L. Mahadevan, “Villification: How the gut gets its villi,” *Science* **342**, 212–218 (2013).

[20] J. Gemmer, E. Sharon, T. Shearman, and S. C. Venkataramani, “Isometric immersions, energy minimization and self-similar buckling in non-Euclidean elastic sheets,” *EPL* **114**, 24003 (2016).

[21] F. Xu, C. Fu, and Y. Yang, “Water affects morphogenesis of growing aquatic plant leaves,” *Phys. Rev. Lett.* **124**, 038003 (2020).

[22] C. Fei, S. Mao, J. Yan, R. Alert, H. A. Stone, B. L. Bassler, N. S. Wingreen, and A. Košmrlj, “Nonuniform growth and surface friction determine bacterial biofilm morphology on soft substrates,” *Proc. Natl. Acad. Sci.* **117**, 7622–7632 (2020).

[23] I. Tobasco, “Curvature-driven wrinkling of thin elastic shells,” to appear in *Arch. Ration. Mech. Anal.*, arXiv:1906.02153.

[24] A.C. Pipkin, “The relaxed energy density for isotropic elastic membranes,” *IMA J. Appl. Math.* **36**, 85–99 (1986).

[25] D. J. Steigmann, “Tension-field theory,” *Proc. Roy. Soc. London Ser. A* **429**, 141–173 (1990).

[26] H. Wagner, “Ebene blechwandträger mit sehr dünnem stegblech,” *Z. Flugtech. Motorluftshifffahrt* **20**, 200 (1929).

[27] Z. Yao, M. Bowick, X. Ma, and R. Sknepnek, “Planar sheets meet negative-curvature liquid interfaces,” *EPL* **101**, 44007 (2013).

[28] J. D. Paulsen, V. Démery, C. D. Santangelo, T. P. Russell, B. Davidovitch, and N. Menon, “Optimal wrapping of liquid droplets with ultrathin sheets,” *Nat. Mater.* **14**, 1206 (2015).

[29] J. D. Paulsen, V. Démery, K. B. Toga, Z. Qiu, T. P. Russell, B. Davidovitch, and N. Menon, “Geometry-driven folding of a floating annular sheet,” *Phys. Rev. Lett.* **118**, 048004 (2017).

[30] M. Ripp, V. Démery, T. Zhang, and J. D. Paulsen, “Geometry underlies the mechanical stiffening and softening of an indented floating film,” *Soft Matter* **16**, 4121–4130 (2020).

[31] A. Braides, *Γ -convergence for beginners* (Oxford University Press, Oxford, 2002).

[32] O. Tovkach, J. Chen, M. M. Ripp, T. Zhang, J. D. Paulsen, and B. Davidovitch, “Mesoscale structure of wrinkle patterns and defect-proliferated liquid crystalline phases,” *Proc. Natl. Acad. Sci.* **117**, 3938–3943 (2020).

[33] J. C. Maxwell, “XLV. On reciprocal figures and diagrams of forces,” *Philos. Mag.* **27**, 250–261 (1864).

[34] S. P. Timoshenko, *History of strength of materials. With a brief account of the history of theory of elasticity and theory of structures* (McGraw-Hill Book Company, Inc., New York-Toronto-London, 1953).

[35] E. Vouga, M. Höbinger, J. Wallner, and H. Pottmann, “Design of self-supporting surfaces,” *ACM Trans. Graph.* **31**, 1–11 (2012).

[36] W. Prager, “On ideal locking materials,” *Trans. Soc. Rheol.* **1**, 169–175 (1957).

[37] Y. C. Fung, “Elasticity of soft tissues in simple elongation,” *Am. J. Physiol.* **213**, 1532–1544 (1967).

[38] W. Prager, “On the formulation of constitutive equations for living soft tissues,” *Q. Appl. Math.* **27**, 128–132 (1969).

[39] H. Elettro, S. Neukirch, F. Vollrath, and A. Antkowiak, “In-drop capillary spooling of spider capture thread inspires hybrid fibers with mixed solid–liquid mechanical properties,” *Proc. Natl. Acad. Sci.* **113**, 6143–6147 (2016).

[40] P. Grandgeorge, N. Krins, A. Hourlier-Fargette, C. Laberty-Robert, S. Neukirch, and A. Antkowiak, “Capillarity-induced folds fuel extreme shape changes in thin wicked membranes,” *Science* **360**, 296–299 (2018).

**Supplementary Information for:
“Exact solutions for the wrinkle patterns of confined elastic shells”**

Tobasco et al.

CONTENTS

I. Supplementary Tables	S2
II. Supplementary Figures	S3
III. Supplementary Text	S5
A. The Lagrange multipliers approach to maximizing coverage	S5
1. Lagrange multipliers and saddle points	S6
2. Minimax procedures for finding saddle points	S7
3. The dual problem for σ_L	S8
4. The Airy potential formulation of the dual	S9
5. Solution formulas, in the abstract	S10
B. Worked examples	S11
1. Negatively curved squares	S11
2. Positively curved squares	S13
C. Derivation of the simple rule set for wrinkles	S16
1. A primer on convex functions	S16
2. The relation between φ_- and φ_+	S18
3. Identifying $\nabla\varphi_-$ and $\nabla\varphi_+$	S19
4. The formulas for σ_L	S20
IV. Materials and Methods	S22
A. Film preparation	S22
B. Finite element simulations	S22
C. Parameter ranges	S22
1. Experimental ranges	S22
2. Simulation ranges	S22
D. Data Availability	S23
References	S23

I. SUPPLEMENTARY TABLES

	Planform shape	$ R_i $ [mm]	t [nm]	W [mm]
Fig. 1a	Square	25, 34	408	5.1
Fig. 3	Triangle	25, 34	331	4.5
	Rectangle	25, 34	242	5.0
	Hexagon	25, 34	334	5.0
	Tangential polygon	25, 34	378	5.9
	Semicircle	25, 34	389	6.3
	Circle	25, 34	427	6.3
	Ellipse	25, 34	325	8.2

TABLE S1. Experimental parameters for the saddle-shaped shell cutouts ($\kappa < 0$) in the main text. Unsigned principal radii of curvature $|R_1|$ and $|R_2|$, thickness t , and initial planar width W are reported.

	Planform shape	R [mm]	t [nm]	W [mm]
Fig. 1b	Square	25.7	167	6.7
Fig. 3	Triangle	34.5	152	6.5
	Rectangle	38.6	162	9.5
	Hexagon	25.7	158	8.4
	Tangential polygon	25.7	166	5.3
	Semicircle	34.5	151	7.7
	Circle	34.5	157	7.7
	Ellipse	25.7	152	8.6

TABLE S2. Experimental parameters for the spherical shell cutouts ($\kappa > 0$) in the main text. Radius of curvature R , thickness t , and initial planar width W are reported. The choice of width depends on the shape. We take it to be a radius, semi-major axis length, or half of a long diagonal or side as appropriate.

	Planform shape	R [cm]	t [μ m]	W [cm]	K [Pa/m]
Fig. 1a	Square ($\kappa < 0$)	6.4, 7.8	1	1	100
Fig. 1b	Square ($\kappa > 0$)	20	5	3.05	2000

TABLE S3. Parameters for the simulated shells in the main text. Radius of curvature R (unsigned principal radii for $\kappa < 0$), thickness t , initial width W , and substrate stiffness K are reported. A Young's modulus of $E = 2$ MPa and Poisson's ratio of $\nu = 0.495$ is used.

II. SUPPLEMENTARY FIGURES

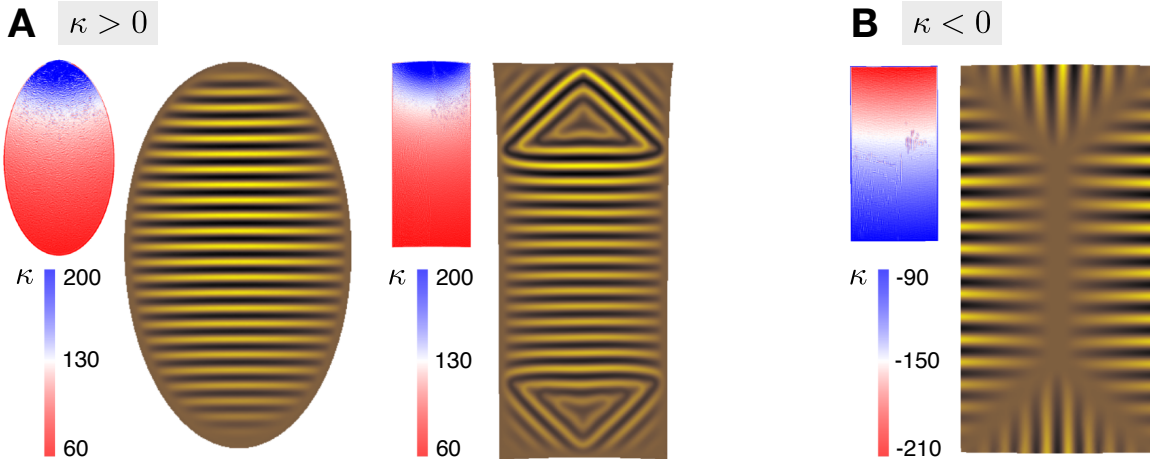


FIG. S1. **Simulated shells with non-constant initial Gaussian curvature of one sign.** Colormaps of the initial Gaussian curvature $\kappa(x)$ of three cut out shells are shown alongside their softly-stamped wrinkled cases. The patterns are largely independent of the precise values of $\kappa(x)$, but depend on its sign. Parameters: (A) $t = 7 \mu\text{m}$, $W = 4 \text{ cm}$ for the ellipse and 3.6 cm for the rectangle, $K = 2000 \text{ Pa/m}$; (B) $t = 2 \mu\text{m}$, $W = 2 \text{ cm}$, $K = 100 \text{ Pa/m}$. Gaussian curvature is in units of cm^{-2} . In both, $E = 2 \text{ MPa}$ and $\nu = 0.495$.

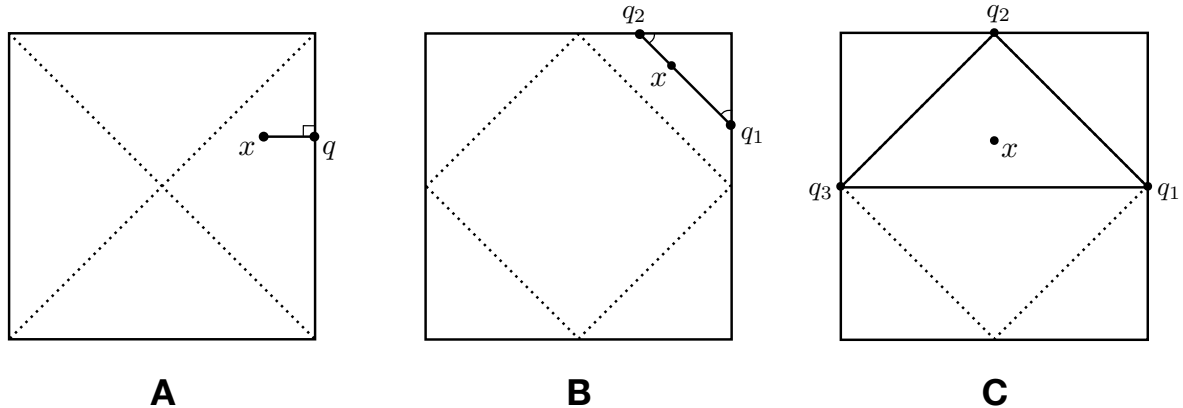


FIG. S2. **Finding the smallest and largest convex extensions of $|x|^2/2$ into a square.** (A): The smallest convex extension $\varphi_-(x)$ is found using a point $q = P_{\partial\Omega}(x)$ closest to x amongst all boundary points. (B-C): The largest convex extension $\varphi_+(x)$ is found by exhibiting x as a convex combination of two optimally-chosen boundary points q_1 and q_2 as in (B), or three optimally-chosen boundary points q_1 , q_2 , and q_3 as in (C).

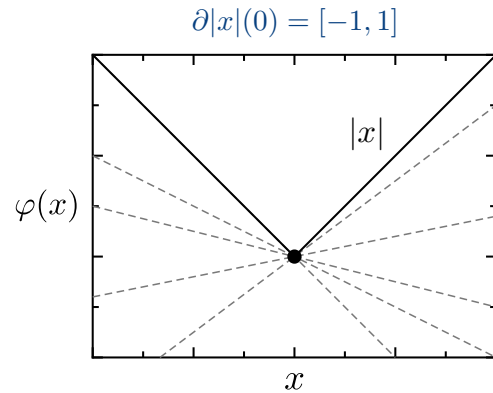


FIG. S3. Demonstration of the subdifferential of a convex function. The subdifferential $\partial|x|(0)$ of the absolute value function $|x|$ at 0 consists of all slopes of tangent lines on or below its graph passing through $(0, 0)$. We use this concept in our derivation of the rules for wrinkles from the main text.

III. SUPPLEMENTARY TEXT

Here we elaborate on our solution of the maximum coverage problem for the wrinkle patterns of confined shallow shells. Section III A begins by recalling some facts obtained by the first author in [S1] which underlie our multipliers-based approach. In Section III B, we discuss the examples of a negatively and a positively curved square. Section III C ends with a complete derivation of our simple rules, which go beyond the examples of [S1] to characterize the wrinkles of general simply connected and negatively or positively curved shallow shells. We have tried to keep the presentation as self-contained as possible. Some references to [S1] appear in the first two sections to avoid going too far into technical details. Besides these, our derivation of the simple rules is self-contained.

Notation. When we write $A \geq 0$ or $A \leq 0$ for a symmetric matrix A , we mean that its eigenvalues are respectively non-negative or non-positive. We say the matrix A is *non-negative* or *non-positive*, correspondingly. We use the matrix inner product

$$A : B = \sum_{i,j} A_{ij} B_{ij}.$$

Note $A \geq 0$ if and only if $A : B \geq 0$ for all $B \geq 0$. The same considerations apply for symmetric matrix-valued functions $S(x)$. To lighten the notation, we often mute the dependence on x , and write $S \geq 0$ or $S \leq 0$ instead of saying explicitly that $S(x) \geq 0$ or $S(x) \leq 0$ for all x .

A. The Lagrange multipliers approach to maximizing coverage

We begin by recalling the general approach to the maximum coverage problem

$$\min_{\varepsilon(u) \leq 0} \Delta A\{u\} \tag{S1}$$

laid out in [S1]. As our shells are shallow, we use the formulas

$$\Delta A\{u\} = \int_{\Omega} \frac{1}{2} \text{tr} M dx - \int_{\partial\Omega} u \cdot \hat{n} ds, \quad \varepsilon(u) = e(u) - \frac{1}{2} M, \quad \text{and} \quad M = \nabla p \otimes \nabla p$$

for the areal change ΔA , the coarse-grained in-plane strain $\varepsilon(u)$, and the misfit $\propto M$. Here, as in the main text, $u = (u_1(x), u_2(x))$ denotes the in-plane displacement of the shell parallel to the plane of the initial water bath, in a limit where its wrinkles are infinitesimally fine and its out-of-plane displacement is vanishingly small. We use $x = (x_1, x_2)$ for the Euclidean coordinate of the initial planar projection $\Omega \subset \mathbb{R}^2$, so that the cutout's mid-shell is initially the graph

$$\{(x_1, x_2, p(x_1, x_2)) : (x_1, x_2) \in \Omega\}$$

of a function $p(x)$. By varying Ω we change the cut out shape; by altering p we control its curvature. Note the initial Gaussian curvature

$$\kappa(x) = \det \nabla \nabla p(x) \tag{S2}$$

to first order in the shallow shell approximation. Although our results hold for non-constant $\kappa(x)$, the constant curvature cases with $p(x) \propto x_1^2 + x_2^2$ and $x_1^2 - x_2^2$ are good examples to keep in mind. These correspond to spherical and saddle-shaped shells. For a quick introduction to shallow shell theory, also called “weakly curved” shell theory, see [S2, Section 4.8].¹

¹ Taking $W = p$ and $w = -p$ in the reference recovers our formula for the strain.

Given this setup, the goals of this section are to (1) obtain the Lagrange multiplier formulation of (S1) on general grounds, and (2) justify the dual problem selecting the multiplier σ_L in the main text. We focus on making the manipulations intuitive, though some technicalities will necessarily arise due to the somewhat unusual nature of the optimization in (S1). Indeed, it is not governed by a smooth potential for which the Euler-Lagrange equations would be straightforward to obtain. Instead, its optimality conditions arise from a careful analysis of σ_L and its relation to $\varepsilon(u)$.

1. Lagrange multipliers and saddle points

The maximum coverage problem (S1) is a constrained minimization over all in-plane displacements $u(x)$ that are tension-free. In our notation, $\varepsilon(u) \leq 0$ meaning its eigenvalues, i.e., the principal strains, are non-positive. Our first step will be to rewrite this one-sided constraint using a Lagrange multiplier $\sigma_L(x)$, which we take henceforth to be a non-negative, two-by-two symmetric matrix-valued function on \mathbb{R}^2 . The reason for extending its domain to the entire plane will be given later on below. For now, we observe that

$$\varepsilon(u) \leq 0 \iff \int_{\Omega} \sigma_L : \varepsilon(u) \leq 0 \quad \forall \sigma_L \geq 0. \quad (\text{S3})$$

This is the way in which the given class of non-negative σ_L enforce the tension-free constraint.

Motivated by this, we introduce the Lagrangian

$$\mathcal{L}\{u, \sigma_L\} = \Delta A\{u\} + \int_{\Omega} \sigma_L : \varepsilon(u) \quad (\text{S4})$$

as in the main text, and consider its critical points under the constraint

$$\sigma_L \geq 0. \quad (\text{S5})$$

The meaning of “criticality” in this context must be addressed, for we do not refer to pairs (u, σ_L) satisfying the usual conditions

$$0 = \frac{\delta \mathcal{L}}{\delta u}\{u, \sigma_L\} = \frac{\delta \mathcal{L}}{\delta \sigma_L}\{u, \sigma_L\}. \quad (\text{S6})$$

Indeed, such points do not include u solving (S1) unless the misfit is *geometrically compatible*, meaning that $\varepsilon(u) = 0$ for some u . For *simply connected* shells, which by definition have no holes, geometric compatibility is equivalent to the Gaussian curvature $\kappa(x)$ vanishing identically throughout, an irrelevant situation from the point of view of geometry-driven wrinkling.

Instead, the correct interpretation of critical points is that of *saddle points*, i.e., (u, σ_L) satisfying

$$\mathcal{L}\{u, \sigma_L + \delta\sigma_L\} \leq \mathcal{L}\{u, \sigma_L\} \leq \mathcal{L}\{u + \delta u, \sigma_L\} \quad (\text{S7})$$

for all variations δu and $\delta\sigma_L$ preserving (S5). By definition, such variations obey

$$\sigma_L + \delta\sigma_L \geq 0. \quad (\text{S8})$$

Simply put, (S7) ensures that \mathcal{L} is minimized in u while it is maximized in σ_L . Its importance lies in the fact that u solves (S1) if and only if there exists a non-negative σ_L satisfying (S7). This was proved recently in [S1], in an application of a so-called minimax theorem from the subject of convex analysis, and we allow ourselves to use it without further justification below. Having explained the utility of saddle points, we turn to the next question: how can one find the saddle points of \mathcal{L} ?

2. Minimax procedures for finding saddle points

Broadly speaking, the saddle points of a given functional, say $\mathcal{L}\{u, \sigma_L\}$, can be recovered through a *minimax* procedure that simultaneously optimizes in u and σ_L . It may help to visualize the landscape of \mathcal{L} nearby a saddle point: a much simplified example is the polynomial in two variables $p(a, b) = -a^2 + b^2$, whose sole saddle point $(0, 0)$ is found by minimizing in a and maximizing in b . While this particular example should not be taken too seriously due to a lack of constraints, the idea is the same. For a general introduction to minimax procedures, see [S3].

We consider two, equivalent minimax procedures applied to \mathcal{L} . Each procedure reveals something new about our problem. Start by considering the following min-max procedure:

$$\min_u \max_{\sigma_L \geq 0} \mathcal{L}\{u, \sigma_L\}.$$

This says to maximize over non-negative σ_L first, then to minimize the result over u . Using (S3), we see that the inner maximum is infinite unless $\varepsilon(u) \leq 0$, in which case

$$\max_{\sigma_L \geq 0} \mathcal{L}\{u, \sigma_L\} = \Delta A\{u\}. \quad (\text{S9})$$

Minimizing, we find that

$$\min_u \max_{\sigma_L \geq 0} \mathcal{L}\{u, \sigma_L\} = \min_{\varepsilon(u) \leq 0} \Delta A\{u\}.$$

Thus, we have recovered (S1) as the min-max of \mathcal{L} . Finding this way of rewriting the maximum coverage problem was the original motivation for introducing σ_L .

Hidden in the previous manipulations is a necessary condition for (u, σ_L) to be a saddle point. For σ_L to be optimal in (S9), it must satisfy

$$0 = \int_{\Omega} \sigma_L : \varepsilon(u)$$

by the definition of \mathcal{L} in (S4). Since $\sigma_L \geq 0$ and $\varepsilon(u) \leq 0$, there follows

$$0 = \sigma_L : \varepsilon(u). \quad (\text{S10})$$

We have arrived at the crucial Eq. (2) of the main text. This is one of two necessary conditions for (u, σ_L) to be a saddle point of \mathcal{L} .

Going onwards, we switch to the other minimax procedure, in which u is minimized over first:

$$\max_{\sigma_L \geq 0} \min_u \mathcal{L}\{u, \sigma_L\}. \quad (\text{S11})$$

This alternative procedure captures the same set of saddle points as the previous min-max one [S1]. However, now that the minimization over u is unconstrained, we can apply the usual critical point condition $0 = \frac{\delta \mathcal{L}}{\delta u}$ to characterize optimal u . Taking variations of (S4) shows u solves

$$\min_u \mathcal{L}\{u, \sigma_L\} \quad (\text{S12})$$

for a given σ_L if and only if

$$0 = - \int_{\partial\Omega} \delta u \cdot \hat{n} \, ds + \int_{\Omega} \sigma_L : e(\delta u) \quad (\text{S13})$$

for all variations δu . This is conveniently simplified by taking

$$\sigma_L(x) = I \quad \text{for } x \notin \Omega \quad (\text{S14})$$

and applying the divergence theorem. Note $-\hat{n}$ is the inwards-pointing unit normal at the boundary. It follows that u is optimal in (S12) if and only if $0 = \int_{\mathbb{R}^2} (\nabla \cdot \sigma_L) \cdot \delta u$ for all δu , i.e., if and only if

$$0 = \nabla \cdot \sigma_L \quad (\text{S15})$$

in the sense just described.

As it turns out, the necessary conditions (S10) and (S15), coupled with the constraints (S5) and (S14), completely characterize the saddle points of \mathcal{L} [S1]. Thus, they are the first order optimality conditions of the original problem (S1). However, the story does not end here, as it is possible to eliminate u so as to turn the analysis of wrinkle patterns into the problem of finding σ_L .

3. The dual problem for σ_L

We proceed to derive the following *dual problem* for the multiplier σ_L , which appears as Eq. (4) in the main text:

$$\max_{\substack{\nabla \cdot \sigma_L = 0 \text{ on } \mathbb{R}^2 \\ \sigma_L \geq 0 \text{ on } \mathbb{R}^2 \\ \sigma_L = I \text{ outside } \Omega}} \int_{\Omega} -\frac{1}{2} M : (\sigma_L - I). \quad (\text{S16})$$

The point is that, together, the solutions of (S1) and (S16) make up the saddle points of \mathcal{L} . Thus, to ascertain optimal u , one may solve the dual problem (S16) for σ_L , and apply the saddle point conditions (S10) and (S15). Actually, the second of these already figures in the maximization, so only the orthogonality condition (S10) must be enforced *a posteriori*.

It should be noted that a maximizer need not satisfy $\sigma_L \hat{n} = \hat{n}$ at $\partial\Omega$, although this does occur in some cases. By taking σ_L to be defined outside of Ω , one allows to maximize over its behavior at $\partial\Omega$ as well. At the present level of generality, this turns out to be crucial to ensure the existence of a maximizer solving (S16). On this point, we refer the reader to [S1] for more details.

We now arrive at (S16) by evaluating the max-min of \mathcal{L} left over from (S11). The inner minimization over u yields the constraint $\nabla \cdot \sigma_L = 0$, as explained in the steps leading up to (S15). We continue to take $\sigma_L = I$ outside Ω . Applying (S13) with $\delta u = u$ then gives that

$$\begin{aligned} \mathcal{L}\{u, \sigma_L\} &= \int_{\Omega} \frac{1}{2} \text{tr} M - \int_{\partial\Omega} u \cdot \hat{n} ds + \int_{\Omega} \sigma_L : \left(e(u) - \frac{1}{2} M \right) \\ &= \int_{\Omega} -\frac{1}{2} M : (\sigma_L - I). \end{aligned}$$

The resulting expression is independent of u , as it should be. Therefore,

$$\max_{\sigma_L \geq 0} \min_u \mathcal{L}\{u, \sigma_L\} = \max_{\substack{\nabla \cdot \sigma_L = 0 \text{ on } \mathbb{R}^2 \\ \sigma_L \geq 0 \text{ on } \mathbb{R}^2 \\ \sigma_L = I \text{ outside } \Omega}} \int_{\Omega} -\frac{1}{2} M : (\sigma_L - I)$$

resulting in (S16).

Both the original maximum coverage problem (S1) and its dual problem (S16) arise from the very same Lagrangian \mathcal{L} . This is one sense in which they are “dual”. A deeper reason is that their optimal values are the same, though this is far from clear. It is tied to the fact used implicitly above, and proved in [S1], that while in principle \mathcal{L} may have more than one saddle point, its value at all of them is the same. Thus, the min-max and max-min procedures are equivalent in the end.

4. The Airy potential formulation of the dual

Having recovered the dual problem for σ_L , we now show how to rewrite it using the Airy-like potentials $\varphi(x)$ in the main text. Introduce the perpendicular gradient

$$\nabla^\perp = (-\partial_2, \partial_1)$$

and make the substitution

$$\sigma_L = \nabla^\perp \nabla^\perp \varphi \quad \text{where} \quad \nabla^\perp \nabla^\perp = \begin{pmatrix} \partial_{22} & -\partial_{12} \\ -\partial_{21} & \partial_{11} \end{pmatrix}. \quad (\text{S17})$$

While the notation $\nabla^\perp \nabla^\perp$ may not be standard, we find it speeds up the required manipulations. For instance, one automatically sees that

$$\nabla \cdot \nabla^\perp = (\partial_1, \partial_2) \cdot (-\partial_2, \partial_1) = 0$$

so that any σ_L obtained via (S17) is divergence-free. It is also symmetric (formally, the derivatives are defined distributionally, in which case $\partial_{12} = \partial_{21}$ always). Our change of variables from σ_L to φ is familiar from the study of planar elasticity problems, and is often referred to as producing the “Airy stress” σ_L associated to the “Airy potential” φ . The potentials we obtain, however, are different from the classical ones as they will turn out to be non-smooth.

We proceed to identify those φ leading to σ_L admissible in the dual. Note the eigenvalues of $\nabla^\perp \nabla^\perp \varphi$ and $\nabla \nabla \varphi$ are equal. Referring to (S16), we see that for φ to be admissible, it must have

$$\nabla \nabla \varphi \geq 0 \quad \text{in } \mathbb{R}^2 \quad \text{and} \quad \nabla \nabla \varphi = I \quad \text{in } \mathbb{R}^2 \setminus \Omega.$$

The first condition requires that φ is a convex function. The second condition shows that

$$\varphi(x) = \frac{1}{2}|x|^2 + a(x) \quad \text{where} \quad \nabla \nabla a(x) = 0 \quad \text{for } x \notin \Omega.$$

Note the abbreviation $|x|^2 = x_1^2 + x_2^2$. If Ω has no holes, we can take $a = 0$ without loss of generality. If Ω has holes, there is the possibility that a is a different affine function within each hole. (See [S1] for more on this.) Proceeding with simply connected shells, we find that the set of admissible σ_L for the dual corresponds to the set of convex functions φ defined on \mathbb{R}^2 and that equal to $|x|^2/2$ for $x \notin \Omega$. As in the main text, we refer to these as *convex extensions* of $|x|^2/2$ into Ω .

Next, we rewrite the integral in (S16) to clarify its dependence on φ . A straightforward calculation using the formula (S2) for the initial Gaussian curvature $\kappa(x)$ reveals that

$$\kappa(x) = -\frac{1}{2} \nabla \times \nabla \times M \quad \text{where} \quad \nabla \times \nabla \times M = \partial_{11} M_{22} + \partial_{22} M_{11} - 2\partial_{12} M_{12}.$$

One checks $\nabla \times \nabla \times$ is the formal adjoint of $\nabla^\perp \nabla^\perp$, i.e., they are related to each other via integration by parts. Integrating by parts twice and ignoring boundary terms for now yields that

$$\begin{aligned} \int_{\Omega} -\frac{1}{2} M : (\sigma_L - I) &= \int_{\Omega} -\frac{1}{2} M : \nabla^\perp \nabla^\perp \left(\varphi - \frac{|x|^2}{2} \right) \\ &= \int_{\Omega} -\frac{1}{2} \nabla \times \nabla \times M \left(\varphi - \frac{|x|^2}{2} \right) = \int_{\Omega} \left(\varphi - \frac{|x|^2}{2} \right) \kappa. \end{aligned}$$

This produces Eq. (6) from the main text, and furnishes an optimization problem for φ wherein the last integral is maximized over all possible convex extensions of $|x|^2/2$ into Ω . Once this optimization is solved, σ_L solving (S16) can be recovered by differentiation.

A word is required about the possibility of boundary terms. For general φ , such terms appear due to the possibility that $\nabla\varphi$ may jump across $\partial\Omega$. Nevertheless, their contributions to the integrals above can be safely ignored, as any φ found via optimization necessarily satisfies an “at-the-boundary” version of the orthogonality in (S10):

$$0 = \hat{n} \cdot [\nabla\varphi] \varepsilon_{\hat{\tau}\hat{\tau}}(u) \quad \text{at } \partial\Omega. \quad (\text{S18})$$

Here, $\hat{n} \cdot [\nabla\varphi]$ is the normal component of the jump in $\nabla\varphi$ across $\partial\Omega$, and $\varepsilon_{\hat{\tau}\hat{\tau}}(u)$ is the $\hat{\tau}\hat{\tau}$ -component of $\varepsilon(u)$ where $\hat{\tau}$ is tangent to $\partial\Omega$. Again, we refer the reader to [S1] for more details.

5. Solution formulas, in the abstract

At this point, we have explained how the dual problem (S16) for the multiplier is equivalent to the following maximization over the Airy-like potentials found above:

$$\max_{\substack{\varphi(x) \text{ is convex} \\ \varphi(x) = |x|^2/2 \text{ outside } \Omega}} \int_{\Omega} \left(\varphi - \frac{|x|^2}{2} \right) \kappa. \quad (\text{S19})$$

The resulting φ informs u solving the maximum coverage problem via the orthogonality conditions, namely (S10) and (S18) using the change of variables (S17) in the former. The remainder of this Supplementary Text clarifies this general result in the special cases when the initial Gaussian curvature $\kappa(x)$ is either > 0 or < 0 throughout. Abstractly, (S19) is then solved by the procedures

$$\varphi_+(x) = \max_{\varphi} \varphi(x) \quad \text{and} \quad \varphi_-(x) = \min_{\varphi} \varphi(x) \quad (\text{S20})$$

where the optimizations are over all convex extensions of $|x|^2/2$ into Ω . Indeed, if $\kappa(x) > 0$, the integral in (S19) is made largest by driving $\varphi(x)$ up to its maximum value. If $\kappa(x) < 0$, one sees to take $\varphi(x)$ as small as possible. From (S17), we recover the formulas

$$\sigma_L(x) = \begin{cases} \nabla^{\perp} \nabla^{\perp} \varphi_-(x) & \kappa(x) < 0 \\ \nabla^{\perp} \nabla^{\perp} \varphi_+(x) & \kappa(x) > 0 \end{cases}$$

for the multipliers of negatively and positively curved shells. To be clear, this formula applies if the initial Gaussian curvature $\kappa(x)$ is of a definite sign.

The previous “solution formulas” for the multiplier are admittedly abstract. Fortunately, they can be greatly simplified to reveal our simple rules. To prepare for Section III C where we perform these manipulations, we now record some partial simplifications from [S1]. The reader interested in the examples of a negatively and a positively curved square may safely skip to Section III B at this point and come back as needed later on.

The first simplification concerns the formula for the smallest convex extension φ_- noted in the main text: given any $x \in \Omega$,

$$\varphi_-(x) = \frac{1}{2}|x|^2 - \frac{1}{2}d_{\partial\Omega}^2(x) \quad \text{where} \quad d_{\partial\Omega}(x) = \min_{q \in \partial\Omega} |x - q|. \quad (\text{S21})$$

Here, $d_{\partial\Omega}(x)$ is the shortest distance from $x \in \Omega$ to the boundary $\partial\Omega$. Underlying (S21) is the fact that every convex function is bounded below by its tangent planes. We give a detailed explanation of this in Section III B 1, focusing on the case of a negatively curved square. In fact, the same reasoning leads to the general formula (S21).

For positively curved shells, we have the following procedure for finding the largest convex extension φ_+ : for any $x \in \Omega$,

$$\varphi_+(x) = \min_{\substack{\{q_i\} \subset \partial\Omega \\ \{\theta_i\} \subset [0,1]}} \sum_i \theta_i \frac{1}{2} |q_i|^2 \quad \text{where} \quad \sum_i \theta_i q_i = x. \quad (\text{S22})$$

The minimization occurs over all ways of writing x as a convex combination of boundary points. In general, at most three q_i are required. Behind (S22) is the fact that φ_+ is the convex hull of

$$h(x) = \begin{cases} \infty & x \in \Omega \\ \frac{1}{2}|x|^2 & x \notin \Omega \end{cases},$$

i.e., the largest convex function that is never larger than h . A brief introduction to convex functions will be given later on in Section III C where we make use of these results.

B. Worked examples

At this point, we have everything we need to derive our rule set for wrinkles. First, however, some examples are in order. Here, we solve for the wrinkles of a square cutout that is either (1) initially negatively curved or (2) initially positively curved, and confined to a plane. To be sure, one could simply appeal to our rules, but instead of doing that we prefer to work through the abstract “solution formulas” from Section III A 5 in the case of a square. Recall the multiplier

$$\sigma_L(x) = \begin{cases} \nabla^\perp \nabla^\perp \varphi_-(x) & \kappa(x) < 0 \\ \nabla^\perp \nabla^\perp \varphi_+(x) & \kappa(x) > 0 \end{cases}$$

where

$$\varphi_-(x) = \min_{\varphi} \varphi(x) \quad \text{and} \quad \varphi_+(x) = \max_{\varphi} \varphi(x).$$

The admissible φ are convex extensions of $|x|^2/2$ into the square reference domain

$$\Omega = \{(x_1, x_2) : |x_1| \leq 1, |x_2| \leq 1\}. \quad (\text{S23})$$

By solving these optimizations, we will obtain the wrinkle patterns of our squares.

The reader may find Fig. 1 from the main text useful in what follows. In particular, we highlight panels (d) and (e), which depict the functions $\varphi_{\pm}(x)$ for the case of a square. Many other examples corresponding to the remaining shells in Fig. 3 are treated in [S1]. Of course, once one has the rules from Section III C, each example becomes straightforward to solve.

1. Negatively curved squares

We start with the negatively curved square. We solve for the smallest convex extension φ_- in two steps: first, we find a way of bounding an arbitrary convex extension φ from below, obtaining

$$\varphi(x) \geq \mathfrak{L}(x) \quad (\text{S24})$$

for some function $\mathfrak{L}(x)$. Different bounding procedures result in different \mathfrak{L} . The optimal procedure we present is characterized by the fact that its $\mathfrak{L}(x)$ is admissible in the dual. There follows

$$\varphi_-(x) = \mathfrak{L}(x) \quad (\text{S25})$$

and this will yield an explicit formula. Panels (c) and (e) of Fig. 1 in the main text illustrate this strategy for finding φ_- . We pursue a similar strategy to recover φ_+ in Section III B 1.

Begin with an arbitrary convex extension φ of $|x|^2/2$ into Ω . Let $x \in \Omega$ and let $q \in \partial\Omega$ be a point that is closest to x amongst all boundary points, as in Fig. S2a. Parameterize the segment xq as $(1-t)x + tq$ for $t \in [0, 1]$, and let

$$f(t) = \varphi((1-t)x + tq).$$

Expanding in a Taylor series around $t = 1$, we get that

$$f(t) = f(1) - f'(1)(1-t) - \int_{s=t}^{s=1} \frac{f''(s)}{2}(t-s) ds$$

for $t \in [0, 1]$. By the boundary conditions for φ ,

$$f(1) = \varphi(q) = \frac{1}{2}|q|^2 \quad \text{and} \quad f'(1) = (q - x) \cdot q.$$

Since φ is convex, so is f and therefore

$$f''(t) \geq 0.$$

From these observations follows the inequality

$$f(t) \geq \frac{1}{2}|q|^2 - (q - x) \cdot q(1-t).$$

Taking $t = 0$ there results

$$\varphi(x) \geq \frac{1}{2}|q|^2 - (q - x) \cdot q = x \cdot q - \frac{1}{2}|q|^2.$$

Note $q = P_{\partial\Omega}(x)$ in the notation from the main text, where $P_{\partial\Omega}(x)$ was introduced as a closest boundary point to x .

In summary, we have shown that an arbitrary convex extension φ must satisfy

$$\varphi(x) \geq \mathfrak{L}(x) := x \cdot P_{\partial\Omega}(x) - \frac{1}{2}|P_{\partial\Omega}(x)|^2$$

for $x \in \Omega$. In fact, the same lower bound holds for general cutouts (we have yet to use that Ω is a square). For the square in (S23),

$$P_{\partial\Omega}(x) = \begin{cases} (1, x_2) & x_1 > 0, -x_1 < x_2 < x_1 \\ (x_1, 1) & x_2 > 0, -x_2 < x_1 < x_2 \\ (-1, x_2) & x_1 < 0, x_1 < x_2 < -x_1 \\ (x_1, -1) & x_2 < 0, x_2 < x_1 < -x_2 \end{cases}. \quad (\text{S26})$$

This proves the anticipated bound (S24), where by default $\mathfrak{L}(x) = |x|^2/2$ for $x \notin \Omega$.

Next, we show that $\varphi_- = \mathfrak{L}$. Again, a similar argument can be used for general cutouts, but we focus the presentation on the case of a square. We check that the bounding function

$$\mathfrak{L}(x) = \begin{cases} x \cdot P_{\partial\Omega}(x) - \frac{1}{2}|P_{\partial\Omega}(x)|^2 & x \in \Omega \\ \frac{1}{2}|x|^2 & x \notin \Omega \end{cases}$$

produced above is itself a convex extension of $|x|^2/2$ into Ω . Evidently, $\mathfrak{L}(x) = |x|^2/2$ outside Ω , so we must only show it is convex. Given $x \in \Omega$, observe

$$(P_{\partial\Omega}(x) - x) \cdot \nabla P_{\partial\Omega}(x) = 0$$

as the closest boundary point to x remains constant along the segment between x and $P_{\partial\Omega}(x)$. So,

$$\nabla \mathfrak{L}(x) = P_{\partial\Omega}(x).$$

Differentiating once more and using (S26), we get for $x \in \Omega$ that

$$\nabla \nabla \mathfrak{L}(x) = \begin{cases} (0, 1) \otimes (0, 1) & x_1 > 0, -x_1 < x_2 < x_1 \\ (-1, 0) \otimes (-1, 0) & x_2 > 0, -x_2 < x_1 < x_2 \\ (0, -1) \otimes (0, -1) & x_1 < 0, x_1 < x_2 < -x_1 \\ (1, 0) \otimes (1, 0) & x_2 < 0, x_2 < x_1 < -x_2 \end{cases}.$$

We write $(q \otimes q')_{ij} = q_i q'_j$ for the outer product of two vectors. As $q \otimes q = (-q) \otimes (-q)$, the signs of the vectors in the products above are immaterial. What matters is that the eigenvalues of $\nabla \nabla \mathfrak{L}$ are non-negative. They are zero and one, and so \mathfrak{L} is indeed convex in each of the four regions listed above. It is not difficult to see that \mathfrak{L} is convex at the boundaries between these regions, as well as at $\partial\Omega$. All this is apparent in Fig. 1e. For the full details, see [S1, Example 6.8].

From the lower bound $\varphi \geq \mathfrak{L}$ and the admissibility of \mathfrak{L} there follows the identity

$$\varphi_-(x) = \mathfrak{L}(x)$$

for all x . Applying the change of variables (S17), which amounts to a rotation, we get the multiplier

$$\sigma_L(x) = \begin{cases} (-1, 0) \otimes (-1, 0) & x_1 > 0, -x_1 < x_2 < x_1 \\ (0, -1) \otimes (0, -1) & x_2 > 0, -x_2 < x_1 < x_2 \\ (1, 0) \otimes (1, 0) & x_1 < 0, x_1 < x_2 < -x_1 \\ (0, 1) \otimes (0, 1) & x_2 < 0, x_2 < x_1 < -x_2 \end{cases}.$$

We are ready to recover the wrinkles. Recall from the main text that any ordered wrinkles align in the limit with the non-null eigenvectors $\hat{T}(x)$ of $\sigma_L(x)$. These are the *stable directions* introduced after Eq. (2). Let us briefly recall the reasoning: since by (S10) the multiplier σ_L is orthogonal to the coarse-grained strain $\varepsilon(u)$, any wrinkles that persist must have peaks and troughs approximately parallel to \hat{T} . Stable directions are only defined up to a sign. Applied here, we find as the stable direction of our negatively curved square

$$\hat{T}(x) = \begin{cases} (-1, 0) & x_1 > 0, -x_1 < x_2 < x_1 \\ (0, -1) & x_2 > 0, -x_2 < x_1 < x_2 \\ (1, 0) & x_1 < 0, x_1 < x_2 < -x_1 \\ (0, 1) & x_2 < 0, x_2 < x_1 < -x_2 \end{cases}.$$

The reader should compare this against the patterns in Fig. 1a of the main text.

2. Positively curved squares

Next, we solve for the wrinkles of the positively curved square. This time, we find the largest convex extension φ_+ of $|x|^2/2$ into Ω . We proceed as above: first, we show an upper bound

$$\varphi(x) \leq \mathfrak{U}(x) \tag{S27}$$

for all convex extensions φ . Then, we check that $\mathfrak{U}(x)$ is itself a convex extension, so that

$$\varphi_+(x) = \mathfrak{U}(x). \quad (\text{S28})$$

This strategy is depicted in Panels (c) and (d) of Fig. 1 in the main text.

Let φ be a convex extension of $|x|^2/2$ into Ω . Decompose Ω into five parts: the isosceles triangles

$$\begin{aligned} T_{\text{ne}} &= \{(x_1, x_2) : x_1 + x_2 > 1, x_1 < 1, x_2 < 1\} \\ T_{\text{nw}} &= \{(x_1, x_2) : -x_1 + x_2 > 1, x_1 > -1, x_2 < 1\} \\ T_{\text{sw}} &= \{(x_1, x_2) : x_1 + x_2 < -1, x_1 > -1, x_2 > -1\} \\ T_{\text{se}} &= \{(x_1, x_2) : -x_1 + x_2 < -1, x_1 < 1, x_2 > -1\} \end{aligned}$$

and the leftover diamond

$$D = \{(x_1, x_2) : |x_1| + |x_2| \leq 1\}.$$

We obtain an upper bound separately in each part. First, let $x \in T_{\text{ne}}$. Abusing notation slightly, we note it belongs to a unique line segment $q_1 q_2$ perpendicular to $(1, 1)$ with $q_1, q_2 \in \partial\Omega$. That is,

$$x = \theta q_1 + (1 - \theta)q_2 \quad \text{where } \theta \in [0, 1].$$

In particular, we can take

$$q_1 = (1, x_1 + x_2 - 1) \quad \text{and} \quad q_2 = (x_1 + x_2 - 1, 1)$$

as in Fig. S2b. Define the function

$$f(\theta) = \varphi(\theta q_1 + (1 - \theta)q_2).$$

The boundary conditions for φ require that

$$f(0) = \varphi(q_1) = \frac{1}{2}|q_1|^2 \quad \text{and} \quad f(1) = \varphi(q_2) = \frac{1}{2}|q_2|^2.$$

Since φ is convex, so is f . Hence,

$$f(\theta) \leq \theta f(0) + (1 - \theta)f(1)$$

for all $\theta \in [0, 1]$. Unpacking the definitions, we conclude that

$$\varphi(x) \leq \theta \frac{|q_1|^2}{2} + (1 - \theta) \frac{|q_2|^2}{2} = \frac{1}{2} (1 + (x_1 + x_2 - 1)^2)$$

for all $x \in T_{\text{ne}}$. This is the desired upper bound (S27) in the triangle T_{ne} . The remaining triangles T_{nw} , T_{sw} , and T_{se} can be dealt with similarly.

If instead $x \in D$, it is a barycenter of a triangle $q_1 q_2 q_3$ with $q_1, q_2, q_3 \in \partial\Omega \cap \partial D$. That is,

$$x = \sum_{i=1}^3 \theta_i q_i \quad \text{where} \quad \sum_{i=1}^3 \theta_i = 1 \quad \text{and} \quad \theta_i \in [0, 1]$$

and where each q_i is a contact point of the inscribed circle to the square. The setup is as depicted in Fig. S2c. By its definition,

$$\varphi(q_i) = \frac{1}{2}|q_i|^2 = \frac{1}{2}$$

for each i . It follows that

$$\varphi(x) \leq \sum_{i=1}^3 \theta_i \frac{1}{2} |q_i|^2 = \frac{1}{2}$$

by convexity. We have proved the upper bound

$$\varphi(x) \leq \mathfrak{U}(x) := \begin{cases} \frac{1}{2}|x|^2 & x \notin \Omega \\ \frac{1}{2}(1 + (x_1 + x_2 - 1)^2) & x \in T_{\text{ne}} \\ \frac{1}{2}(1 + (-x_1 + x_2 - 1)^2) & x \in T_{\text{nw}} \\ \frac{1}{2}(1 + (-x_1 - x_2 - 1)^2) & x \in T_{\text{sw}} \\ \frac{1}{2}(1 + (x_1 - x_2 - 1)^2) & x \in T_{\text{se}} \\ \frac{1}{2} & x \in D \end{cases}$$

anticipated in (S27). Note we took $\mathfrak{U}(x) = |x|^2/2$ by default for $x \notin \Omega$.

The next step is to check that \mathfrak{U} is a convex extension of $|x|^2/2$ into Ω . It is obviously equal to $|x|^2/2$ outside Ω , so we only need to verify it is convex. For $x \in \Omega$, we see that

$$\nabla \nabla \mathfrak{U}(x) = \begin{cases} (1, 1) \otimes (1, 1) & x \in T_{\text{ne}} \\ (-1, 1) \otimes (-1, 1) & x \in T_{\text{nw}} \\ (-1, -1) \otimes (-1, -1) & x \in T_{\text{sw}} \\ (1, -1) \otimes (1, -1) & x \in T_{\text{se}} \\ 0 & x \in D \end{cases}.$$

Note $\nabla \nabla \mathfrak{U}(x)$ either has one non-negative eigenvalue, or is equal to zero. In any case, $\nabla \nabla \mathfrak{U} \geq 0$ so that \mathfrak{U} is convex. Again, one must be a bit more careful to check its convexity at $\partial\Omega$, but this is not so difficult to do and we refer to [S1, Example 6.3] for the full details.

Having shown the upper bound $\varphi \leq \mathfrak{U}$ and concluded that \mathfrak{U} is convex, we get the formula

$$\varphi_+(x) = \mathfrak{U}(x)$$

for all x . Applying (S17), which again amounts to a rotation, we produce the multiplier

$$\sigma_L(x) = \begin{cases} (-1, 1) \otimes (-1, 1) & x \in T_{\text{ne}} \\ (-1, -1) \otimes (-1, -1) & x \in T_{\text{nw}} \\ (1, -1) \otimes (1, -1) & x \in T_{\text{sw}} \\ (1, 1) \otimes (1, 1) & x \in T_{\text{se}} \\ 0 & x \in D \end{cases}.$$

The ordered wrinkles of our positively curved square are therefore shown to have their peaks and troughs parallel to the stable direction

$$\hat{T}(x) = \begin{cases} \left(-\frac{1}{\sqrt{2}}, \frac{1}{\sqrt{2}}\right) & x \in T_{\text{ne}} \\ \left(-\frac{1}{\sqrt{2}}, -\frac{1}{\sqrt{2}}\right) & x \in T_{\text{nw}} \\ \left(\frac{1}{\sqrt{2}}, -\frac{1}{\sqrt{2}}\right) & x \in T_{\text{sw}} \\ \left(\frac{1}{\sqrt{2}}, \frac{1}{\sqrt{2}}\right) & x \in T_{\text{se}} \end{cases}.$$

Since $\sigma_L = 0$ in the diamond D , it admits no non-null eigenvectors and hence no stable directions there. This marks the possibility of a disordered response. The reader should compare these results against the patterns in Fig. 1b of the main text.

C. Derivation of the simple rule set for wrinkles

The previous sections explained our approach to predicting the wrinkle patterns of confined shallow shells, and demonstrated it for a positively and negatively curved square. The key quantity of interest is the multiplier σ_L solving the dual problem (S16). Its non-null eigenvectors are the stable directions of the shell. Recall that, due to the orthogonality of σ_L and the coarse-grained strain $\varepsilon(u)$, such directions point along the ordered peaks and troughs. We now obtain a far-reaching simplification of this result. We establish the following rules, which apply whenever the shell is simply connected and if its initial Gaussian curvature $\kappa(x)$ is of one sign:

- (i) If $\kappa(x) < 0$, the shell's ordered wrinkles are predicted to fall along segments of quickest exit from the planar projection Ω of the shell. Such paths are line segments that meet the boundary $\partial\Omega$ perpendicularly, and meet each other at the medial axis \mathfrak{M} of Ω .
- (ii) If $\kappa(x) > 0$, the shell's ordered wrinkles are predicted to fall along a distinguished family of line segments connecting pairs of boundary points $\{q, r\} \subset \partial\Omega$. Each such pair arises as the unique closest boundary points to some $p \in \mathfrak{M}$.
- (iii) If $\kappa(x) > 0$, any disorder that occurs is predicted to reside within a family of convex regions, constructed using the points on the medial axis leftover from the previous rule. Each such region is the convex hull of three or more closest boundary points to some $p \in \mathfrak{M}$.

Recall the *convex hull* of $Q \subset \mathbb{R}^2$ is the smallest subset of \mathbb{R}^2 that contains Q and has the property that if it contains the points q and r , it contains the line segment qr between them. We write $\text{co } Q$ for the convex hull of Q . Together, rules (i) and (ii) constitute one of the two reciprocal pairings in the main text: the ordered wrinkles of negatively and positively curved shells pair via isosceles triangles. Rule (iii) pairs the disordered regions of positively curved shells with certain families of ordered wrinkles in their negatively curved counterparts. See Fig. 2 of the main text.

Here, we derive these rules by elaborating on the strategy at the end of the main text. We seek the following formulas for the multiplier asserted in Eqs. (7) and (8) there:

$$\sigma_L(x) = \begin{cases} R^T \nabla P_{\partial\Omega}(x) R & \kappa(x) < 0 \\ R^T \nabla P_{\mathfrak{M}}(x) R & \kappa(x) > 0 \end{cases} \quad (\text{S29})$$

where $P_{\partial\Omega}$ and $P_{\mathfrak{M}}$ are as in the main text (for their precise definitions, see Section III C 3). We break the argument into three steps, given in Section III C 2-Section III C 4. The predicted stable directions, and the stated rules, follow at the very end. Section III C 1 is a primer on convex functions for the reader who might be unfamiliar with such concepts as the subdifferential. We assume the reader is familiar with Section III A 5, and especially with the formulas (S21) and (S22) for the smallest and largest convex extensions $\varphi_-(x)$ and $\varphi_+(x)$ of $|x|^2/2$ into Ω .

1. A primer on convex functions

The following facts about convex functions are used to derive (S29). For our purposes, we state them for functions defined on \mathbb{R}^2 . Their proofs appear in various textbooks on convex analysis and related subjects (see, e.g., [S4, S5]).

Recall a function $\varphi(x)$ defined for $x \in \mathbb{R}^2$ is said to be *convex* if

$$\varphi(\theta x + (1 - \theta)y) \leq \theta\varphi(x) + (1 - \theta)\varphi(y)$$

for all $x, y \in \mathbb{R}^2$ and $\theta \in [0, 1]$. Geometrically, this says that the graph of φ lies on or below any line segment connecting two of its points. For smooth φ , convexity is equivalent to the condition that $\nabla \nabla \varphi \geq 0$, meaning its eigenvalues are non-negative. In fact, this equivalence holds more generally, provided the second derivatives of φ are interpreted in a suitable (distributional) sense.

While a general convex function $\varphi(x)$ need not be smooth, it will be differentiable at almost every x . Precisely, the set of exceptional points where φ is not differentiable is of measure zero. Examples of zero area sets in the plane are smooth curves. Even if φ fails to be differentiable at x , one can still define the notion of a “tangent plane” to its graph. In general, there can be multiple tangent planes at $(x, \varphi(x))$. The usual convention, which we follow here, is to refer to those that lie on or below the graph of φ . Correspondingly, we define the *subdifferential* of φ at x as the set

$$\partial \varphi(x) = \{p \in \mathbb{R}^2 : \varphi(y) \geq \varphi(x) + p \cdot (y - x) \text{ for all } y \in \mathbb{R}^2\}.$$

Points $p \in \partial \varphi(x)$ correspond to tangent planes. Conveniently, φ is differentiable at x in the usual sense if and only if $\partial \varphi(x)$ consists of a single point, in which case $\partial \varphi(x) = \{\nabla \varphi(x)\}$. See Fig. S3 for an illustrative one-dimensional example.

Next, we recall the *Legendre transform* of a function $\varphi(x)$, which at this stage is not required to be convex. This is the function $\varphi^*(p)$ defined for $p \in \mathbb{R}^2$ by

$$\varphi^*(p) = \max_{x \in \mathbb{R}^2} x \cdot p - \varphi(x).$$

Even if a maximizing x does not exist, the value of $\varphi^*(p)$ can still be defined (it may be ∞). One checks that φ^* is convex, regardless of the convexity of φ . If φ is convex, its subdifferential and that of its Legendre transform are related in the following way:

$$p \in \partial \varphi(x) \iff x \in \partial \varphi^*(p). \quad (\text{S30})$$

Such pairs (x, p) are equivalently characterized by the statement that

$$\varphi(x) + \varphi^*(p) = x \cdot p.$$

The subdifferentials of the convex functions φ_- and φ_+ form the backbone of our reciprocal rules for wrinkles, as will become clear.

Finally, we explain the *double Legendre transform* of φ , also known as its *biconjugate*:

$$\varphi^{**} = (\varphi^*)^*.$$

For general φ , which may even take on the value ∞ , there always holds

$$\varphi(x) \geq \varphi^{**}(x). \quad (\text{S31})$$

Note φ^{**} is convex, and (S31) ensures its graph lies on or beneath that of φ . Actually, a stronger statement is true: under certain technical conditions,² which can be checked to hold in our applications of this result below, φ^{**} is the *convex hull* of φ , i.e., the largest convex function that is never larger than φ . In symbols,

$$\varphi^{**}(x) = \max_{\psi} \psi(x)$$

where the maximization is over all convex functions ψ satisfying $\psi \leq \varphi$. In particular, $\varphi = \varphi^{**}$ if and only if φ is convex, under the same technical conditions.

² It is sufficient that the convex hull of φ be lower semicontinuous, and that it does not take on the value $-\infty$.

2. *The relation between φ_- and φ_+*

We begin the proof of the formulas (S29) for the multipliers of our negatively and positively curved shells. The first step is to realize that the smallest and largest convex extensions $\varphi_-(x)$ and $\varphi_+(x)$ of $|x|^2/2$ into Ω are Legendre transforms of one another:

$$\varphi_+ = \varphi_-^* \quad \text{and} \quad \varphi_- = \varphi_+^*. \quad (\text{S32})$$

Our plan is to establish the first part of (S32) directly, and then to make use of the double Legendre transform recalled above.

In Section III A 5 we noted that φ_+ is the convex hull of

$$h(x) = \begin{cases} \infty & x \in \Omega \\ \frac{1}{2}|x|^2 & x \notin \Omega \end{cases}.$$

Using the Legendre transform, we now write this as

$$\varphi_+ = h^{**}. \quad (\text{S33})$$

Separately, we observe that

$$\varphi_- = h^*. \quad (\text{S34})$$

Indeed, if $x \in \Omega$ then the shortest distance from it to the boundary satisfies

$$d_{\partial\Omega}(x) = \min_{y \in \partial\Omega} |x - y| = \min_{y \notin \Omega} |x - y|,$$

as the points in $\partial\Omega$ are closer to x than any other point outside of Ω . By (S21),

$$\begin{aligned} \varphi_-(x) &= \frac{1}{2}|x|^2 - \frac{1}{2}d_{\partial\Omega}^2(x) = \frac{1}{2}|x|^2 - \frac{1}{2}\min_{y \notin \Omega} |x - y|^2 \\ &= \max_{y \notin \Omega} \frac{1}{2}|x|^2 - \frac{1}{2}|x - y|^2 = \max_{y \notin \Omega} x \cdot y - \frac{1}{2}|y|^2 \\ &= \max_{y \in \mathbb{R}^2} x \cdot y - h(y) = h^*(x). \end{aligned}$$

If, on the other hand, $x \notin \Omega$ then a straightforward manipulation using the definitions, along with the fact that $|x|^2/2$ is its own Legendre transform, shows that both $\varphi_-(x)$ and $h^*(x)$ equal $|x|^2/2$.

Combining (S34) with (S33), we see that

$$\varphi_+ = (h^*)^* = \varphi_-^*.$$

Since φ_- is convex it follows immediately that

$$\varphi_- = \varphi_-^{**} = \varphi_+^*.$$

We have shown (S32). For future use, note the following result:

$$p \in \partial\varphi_+(x) \iff x \in \partial\varphi_-(p) \iff \varphi_+(x) + \varphi_-(p) = x \cdot p. \quad (\text{S35})$$

These equivalences are a direct consequence of the discussion surrounding (S30) and the fact that φ_+ and φ_- are Legendre transforms of one another.

3. Identifying $\nabla\varphi_-$ and $\nabla\varphi_+$

The second step is to show that

$$\nabla\varphi_- = P_{\partial\Omega} \quad \text{and} \quad \nabla\varphi_+ = P_{\mathfrak{M}} \quad (\text{S36})$$

almost everywhere in Ω (albeit with different sets of exceptional points). This is probably the hardest step in our proof of (S29). First, we clarify the definitions of $P_{\partial\Omega}$ and $P_{\mathfrak{M}}$, both of which map Ω to certain subsets thereof. The reader may wish to consult Fig. 2 in the main text.

The former is defined by the condition that $P_{\partial\Omega}(x)$ is a closest boundary point to x :

$$P_{\partial\Omega}(x) \in \partial\Omega \quad \text{and} \quad d_{\partial\Omega}(x) = |x - P_{\partial\Omega}(x)|. \quad (\text{S37})$$

Almost every $x \in \Omega$ has a unique closest boundary point. The exceptional points to this rule are where $P_{\partial\Omega}$ is not uniquely defined, as they admit multiple closest boundary points. Such points belong to the *medial axis* of Ω , which by definition is the set

$$\mathfrak{M} = \{p \in \Omega : d_{\partial\Omega}(p) = |p - q| \text{ for multiple } q \in \partial\Omega\}.$$

This set appears in white in the $\kappa < 0$ shells of Figs. 1-3 of the main text.

Next, we define $P_{\mathfrak{M}}$. Given $p \in \Omega$, we first associate to it the set of its closest boundary points,

$$Q_p = \{q \in \partial\Omega : d_{\partial\Omega}(p) = |p - q|\}.$$

Evidently, Q_p contains two or more points if and only if $p \in \mathfrak{M}$. With this, we let $P_{\mathfrak{M}}(x)$ be a point on the medial axis whose closest boundary points have x in their convex hull:

$$P_{\mathfrak{M}}(x) \in \mathfrak{M} \quad \text{and} \quad x \in \text{co } Q_{P_{\mathfrak{M}}(x)}. \quad (\text{S38})$$

Again, $P_{\mathfrak{M}}$ is uniquely defined almost everywhere in Ω ; in some rare instances x may belong to multiple convex hulls. Fig. 2b,e in the main text shows a couple typical cases, in which Q_p consists of two and four boundary points, respectively.

We are ready to establish (S36). First, recall from (S21) the formula

$$\varphi_-(x) = \frac{1}{2}|x|^2 - \frac{1}{2}d_{\partial\Omega}^2(x)$$

for $x \in \Omega$. Differentiating almost everywhere yields that

$$\nabla\varphi_-(x) = x - d_{\partial\Omega}(x)\nabla d_{\partial\Omega}(x).$$

The unit vector $-\nabla d_{\partial\Omega}(x)$ points in the direction of steepest decrease of the shortest distance to the boundary. Hence, $x - d_{\partial\Omega}\nabla d_{\partial\Omega}(x)$ is a closest boundary point to x . From (S37), we get that

$$\nabla\varphi_-(x) = P_{\partial\Omega}(x)$$

almost everywhere. This explains the first part of (S36).

We turn to $\nabla\varphi_+$. This time, we make use of the relationship between the subdifferentials $\partial\varphi_+$ and $\partial\varphi_-$ obtained at the end of Section III C 2. As φ_+ is convex,

$$\partial\varphi_+(x) = \{\nabla\varphi_+(x)\}$$

for almost every x . For such x , the first equivalence in (S35) simplifies to the statement that

$$x \in \partial\varphi_-(\nabla\varphi_+(x)). \quad (\text{S39})$$

We proceed to identify the subdifferential of φ_- .

Let $p \in \Omega$. The fact is that $\partial\varphi_-(p)$ is the convex hull of the closest boundary points to p , i.e., the set called $\text{co } Q_p$. To justify this, we turn to the second equivalence in (S35). Using (S22), we get that $x \in \partial\varphi_-(p)$ if and only if

$$\begin{aligned}\varphi_-(p) &= x \cdot p - \varphi_+(x) = x \cdot p - \min_{\sum \theta_i q_i = x} \sum \theta_i \frac{1}{2} |q_i|^2 \\ &= x \cdot p - \min_{\sum \theta_i q_i = x} \sum \theta_i \left(\frac{1}{2} |q_i - p|^2 + (q_i - p) \cdot p + \frac{1}{2} |p|^2 \right) \\ &= \frac{1}{2} |p|^2 - \frac{1}{2} \min_{\sum \theta_i q_i = x} \sum \theta_i |q_i - p|^2.\end{aligned}$$

Each minimization takes place over all finite sets of boundary points $\{q_i\} \subset \partial\Omega$ satisfying

$$x = \sum_i \theta_i q_i \quad \text{where} \quad \sum_i \theta_i = 1 \quad \text{and} \quad \theta_i \in [0, 1].$$

Once the q_i are chosen, the weights θ_i can be determined. Using (S21), we get that

$$x \in \partial\varphi_-(p) \iff d_{\partial\Omega}^2(p) = \min_{\sum \theta_i q_i = x} \sum \theta_i |p - q_i|^2. \quad (\text{S40})$$

Such x are apparently a convex combination of optimally chosen boundary points. General $q_i \in \partial\Omega$ satisfy $d_{\partial\Omega}(p) \leq |p - q_i|$. Optimal q_i are therefore characterized by the condition that

$$d_{\partial\Omega}(p) = |p - q_i| \quad \text{for each } i.$$

We have shown for $p \in \Omega$ that $x \in \partial\varphi_-(p)$ if and only if x is a convex combination of closest boundary points to p . Hence,

$$\partial\varphi_-(p) = \text{co } Q_p \quad (\text{S41})$$

by the definition of Q_p .

Together, (S39) and (S41) reveal for almost every $x \in \Omega$ that

$$\nabla\varphi_+(x) \in \mathfrak{M} \quad \text{and} \quad x \in \text{co } Q_{\nabla\varphi_+(x)}.$$

Indeed, the first condition follows from the second one for x interior to Ω . Recall $P_{\mathfrak{M}}$ was defined in (S38) precisely such that these conditions would hold. Putting it all together, we deduce that

$$\nabla\varphi_+(x) = P_{\mathfrak{M}}(x)$$

almost everywhere. The proof of (S36) is complete.

4. The formulas for σ_L

We are ready to conclude the formulas for σ_L in (S29), and to establish our simple rules. From Section III A 5, we know that

$$\sigma_L = \begin{cases} \nabla^\perp \nabla^\perp \varphi_- & \kappa(x) \leq 0 \\ \nabla^\perp \nabla^\perp \varphi_+ & \kappa(x) \geq 0 \end{cases} \quad (\text{S42})$$

where $\varphi_-(x)$ and $\varphi_+(x)$ are the largest and smallest convex extensions of $|x|^2/2$ into Ω . Their first derivatives were identified in Section III C 3, with the result being (S36). Recall those formulas hold almost everywhere in Ω . Differentiating once more, we get that

$$\nabla \nabla \varphi_- = \nabla P_{\partial\Omega} \quad \text{and} \quad \nabla \nabla \varphi_+ = \nabla P_{\mathfrak{M}}$$

again almost everywhere. We proceed to solve for σ_L .

Recall the notation $\nabla^\perp \nabla^\perp$ from (S17). The required rotations can be done using

$$R = \begin{pmatrix} 0 & -1 \\ 1 & 0 \end{pmatrix}$$

and the observation that

$$\nabla^\perp \nabla^\perp = \begin{pmatrix} \partial_{22} & -\partial_{12} \\ -\partial_{21} & \partial_{11} \end{pmatrix} = R^T \begin{pmatrix} \partial_{11} & \partial_{12} \\ \partial_{21} & \partial_{22} \end{pmatrix} R = R^T (\nabla \nabla) R.$$

Hence,

$$\nabla^\perp \nabla^\perp \varphi_- = R^T \nabla P_{\partial\Omega} R \quad \text{and} \quad \nabla^\perp \nabla^\perp \varphi_+ = R^T \nabla P_{\mathfrak{M}} R. \quad (\text{S43})$$

Combining (S42) and (S43) proves that

$$\sigma_L = \begin{cases} R^T \nabla P_{\partial\Omega} R & \kappa(x) < 0 \\ R^T \nabla P_{\mathfrak{M}} R & \kappa(x) > 0 \end{cases} \quad (\text{S44})$$

as originally claimed.

This remarkably concise formula encodes the mapping from the choice of cutout to the wrinkle patterns it makes upon the plane. The link is furnished by the stable directions introduced in the main text immediately after Eq. (2), and which point along the ordered wrinkle peaks and troughs. By definition, the stable directions \hat{T}_- and \hat{T}_+ of our negatively and positively curved cutouts are non-null unit eigenvectors of their corresponding multipliers, given in (S44). Thus,

$$\hat{T}_- \times \nabla P_{\partial\Omega} \neq 0 \quad \text{and} \quad \hat{T}_+ \times \nabla P_{\mathfrak{M}} \neq 0.$$

From their definitions at the top of Section III C 3, both $P_{\partial\Omega}(x)$ and $P_{\mathfrak{M}}(x)$ are constant along at least one line segment through each x where they are defined. Therefore, $\nabla P_{\partial\Omega}$ and $\nabla P_{\mathfrak{M}}$ are at most rank one, almost everywhere. They are also symmetric, as they are rotated versions of $\nabla \nabla \varphi_-$ and $\nabla \nabla \varphi_+$. So, an equivalent characterization of \hat{T}_- and \hat{T}_+ is that

$$\hat{T}_- \cdot \nabla P_{\partial\Omega} = 0 \quad \text{and} \quad \hat{T}_+ \cdot \nabla P_{\mathfrak{M}} = 0, \quad (\text{S45})$$

as noted in the main text.

Rules (i)-(iii) at the start of this section summarize the content of (S45). The first rule asserts the ordered wrinkles of negatively curved shells follow paths of quickest exit from Ω . Indeed, $\hat{T}_-(x)$ points along the line segment between x and $P_{\partial\Omega}(x)$, as $P_{\partial\Omega}$ is constant there. At the same time, $\hat{T}_+(x)$ is along the segment between the two closest boundary points to $P_{\mathfrak{M}}(x)$, in regions where $\nabla P_{\mathfrak{M}} \neq 0$. This is a special case of (S38) combined with (S45), and so rule (ii) is proved. The last rule concerns the disordered regions of positively curved shells. These are captured by the remaining case of (S38), where $P_{\mathfrak{M}}(x)$ admits three or more closest boundary points. Evidently, $P_{\mathfrak{M}}$ is constant throughout their convex hull. Hence, $\sigma_L = 0$ there, marking the possibility of a disordered response. This completes the proofs of our simple rules.

IV. MATERIALS AND METHODS

A. Film preparation

We spin-coat solutions of polystyrene in toluene onto glass substrates of various positive and negative Gaussian curvatures. Film thickness is varied by changing the polymer concentration (1 to 5% by mass) and spinning speed (2000 to 4000 rpm). Different shapes are cut out using a metal scribe. After preparing the glass substrates with a thin layer of poly(acrylic acid), the films are released by dissolving this sacrificial layer in water. The films are finally transferred to a pure water-air interface. Following the experiments, each film is captured and its thickness is measured using a white-light interferometer (Filmetrics F3).

B. Finite element simulations

Simulations of shells bonded to a planar liquid substrate without surface tension are performed using the finite element package ABAQUS/Explicit. Four-node thin shell elements with reduced integration (element type S4R) are used. The confining force is specified as a non-uniform distributed pressure load over the surface of the shell, via a VDLOAD subroutine. Free boundary conditions are used. Comparative non-linear geometric finite element analysis using both linearly elastic and neo-Hookean hyperelastic materials show the results are largely independent of the model. Color-coding in the images correspond to vertical deflections from the plane.

C. Parameter ranges

Here we report the parameter ranges of the 111 experiments and several hundred simulations in our study. For specific parameters corresponding to the images in the main text and in Section II, see the tables in Section I and the figure captions, respectively. We use the following dimensionless groups to report the ranges: the inverse bendability $b = BR^2/YW^4$, the inverse deformability $k = KR^2/Y$, and the inverse confinement $\gamma = \gamma_{lv}R^2/YW^2$ [S1, S6].

1. Experimental ranges

The shells are shallow with $0.01 < (W/R)^2 < 0.2$ and highly bendable with $4 \times 10^{-11} < b < 2 \times 10^{-8}$. The substrate has non-dimensional stiffness $0.003 < k < 0.03$. The experiments satisfy

$$10^{-2} < \frac{\gamma}{k} < 0.7, \quad 10^{-6} < 2\sqrt{bk} < 3 \times 10^{-5},$$

$$4 \times 10^{-4} < \gamma < 10^{-2}, \quad 10^{-3} < (b/k)^{1/4} < 10^{-1}.$$

2. Simulation ranges

The shells are shallow with $0.01 < (W/R)^2 < 0.04$ and highly bendable with $7 \times 10^{-9} < b < 2 \times 10^{-6}$. The substrate has non-dimensional stiffness $6 < k < 40$. The simulations satisfy

$$\frac{\gamma}{k} = 0, \quad 2 \times 10^{-4} < 2\sqrt{bk} < 2 \times 10^{-2},$$

$$\gamma = 0, \quad 5.6 \times 10^{-3} < (b/k)^{1/4} < 10^{-2}.$$

D. Data Availability

The data that support the findings of this study are available from the corresponding authors upon reasonable request.

- [S1] I. Tobasco, “Curvature-driven wrinkling of thin elastic shells,” to appear in *Arch. Ration. Mech. Anal.*, arXiv:1906.02153.
- [S2] P. Howell, G. Kozyreff, and J. Ockendon, *Applied solid mechanics* (Cambridge University Press, Cambridge, 2009).
- [S3] I. Ekeland and R. Témam, *Convex analysis and variational problems*, Classics in Applied Mathematics, Vol. 28 (Society for Industrial and Applied Mathematics, Philadelphia, PA, 1999).
- [S4] R. T. Rockafellar, *Convex analysis*, Princeton Mathematical Series, No. 28 (Princeton University Press, Princeton, N.J., 1970).
- [S5] B. Dacorogna, *Direct methods in the calculus of variations*, 2nd ed., Applied Mathematical Sciences, Vol. 78 (Springer, New York, 2008).
- [S6] E. Hohlfeld and B. Davidovitch, “Sheet on a deformable sphere: Wrinkle patterns suppress curvature-induced delamination,” *Phys. Rev. E* **91**, 012407 (2015).